nature physics

ARTICLES

https://doi.org/10.1038/s41567-021-01219-x

Check for updates

Two-fold symmetric superconductivity in few-layer $NbSe_2$

Alex Hamill[1,8], Brett Heischmidt[1,8], Egon Sohn[2,3,8], Daniel Shaffer[1], Kan-Ting Tsai[1], Xi Zhang[1], Xiaoxiang Xi[4], Alexey Suslov[5], Helmuth Berger[6], László Forró[6], Fiona J. Burnell[1], Jie Shan[3,7], Kin Fai Mak[3,7], Rafael M. Fernandes[1], Ke Wang[1]✉ and Vlad S. Pribiag[1]✉

The strong Ising spin–orbit coupling in certain two-dimensional transition metal dichalcogenides can profoundly affect the superconducting state in few-layer samples. For example, in $NbSe_2$, this effect combines with the reduced dimensionality to stabilize the superconducting state against magnetic fields up to ~35 T, and could lead to topological superconductivity. Here we report a two-fold rotational symmetry of the superconducting state in few-layer $NbSe_2$ under in-plane external magnetic fields, in contrast to the three-fold symmetry of the lattice. Both the magnetoresistance and critical field exhibit this two-fold symmetry, and it also manifests deep inside the superconducting state in $NbSe_2/CrBr_3$ superconductor-magnet tunnel junctions. In both cases, the anisotropy vanishes in the normal state, demonstrating that it is an intrinsic property of the superconducting phase. We attribute the behaviour to the mixing between two closely competing pairing instabilities, namely the conventional *s*-wave instability typical of bulk $NbSe_2$ and an unconventional *d*- or *p*-wave channel that emerges in few-layer $NbSe_2$. Our results demonstrate the unconventional character of the pairing interaction in few-layer transition metal dichalcogenides and highlight the exotic superconductivity in this family of two-dimensional materials.

In the conventional Bardeen–Cooper–Schrieffer (BCS) theory of superconductivity, the pairing state is characterized by the breaking of a U(1) symmetry related to fixing the phases of the Cooper-pairs wavefunction. Yet, several superconductors break additional symmetries, leading to new forms of superconductivity. Symmetry-breaking in a superconductor may arise through intrinsically anisotropic pairing channels, as well as through coupling between different channels promoted by external perturbations. Hexagonal $NbSe_2$ is a superconducting[1] member of the transition metal dichalcogenide (TMD) family, a class of materials that has been attracting major interest[2–9] because of the range of properties they exhibit, such as layer-dependent inversion symmetry, valley-contrasted Berry curvatures and strong spin–orbit coupling (SOC). $NbSe_2$ exhibits superconductivity and charge density wave order[10–12] from bulk to monolayer forms. In bulk, $NbSe_2$ is believed to be in the *s*-wave pairing state[13]. However, in few-layer hexagonally stacked 2H-$NbSe_2$, the underlying crystalline symmetries give rise to distinct electronic properties. For example, odd-layer-number $NbSe_2$ lacks inversion symmetry (Fig. 1a,b), which leads to a spin–orbit interaction that polarizes the spins of different valleys in different out-of-plane directions[8], as illustrated by the Fermi surface plotted in Fig. 1c. This so-called Ising SOC stabilizes the superconducting state against in-plane magnetic fields far exceeding the Pauli paramagnetic limit[8,14] imposed by conventional superconducting theory[15,16]. This effect becomes stronger as the monolayer limit is approached[8,14]. In addition to Ising superconductivity, other unique superconducting properties such as field-induced mixed-parity states[17,18] and topological superconductivity have been theoretically proposed[19–25] in TMDs. However, other than the stability of the superconducting state against high fields, little is known experimentally about the nature and symmetry of the pairing state in the few-layer limit.

In this work, we report two-fold-periodic superconducting properties of few-layer encapsulated $NbSe_2$ samples studied under rotating in-plane magnetic fields. This periodicity is confirmed by three complementary experimental approaches: magneto-transport near the transition temperature (T_c), measurements of the effective critical field ($\tilde{H}_c$) and tunnelling across magnetic tunnel junctions deep inside the superconducting state. The superconducting properties follow a $\cos(2\theta)$ dependence on the in-plane field angle as probed with all three experimental approaches. This oscillation shows a dominant correlation with the long, straight edge of the $NbSe_2$ flake. The observation of this phenomenon using both magneto-transport and tunnelling devices highlights its intrinsic nature, which persists in distinct device architectures and under very different probing processes. These results are suggestive of field- or strain-induced mixing between quasi-degenerate pairing states with *s*-wave and *d*- or *p*-wave symmetries in few-layer samples, thus shedding new light on the unusual superconducting state of few-layer TMDs.

Figure 1d shows device 1 (schematic, Fig. 1e), a hexagonal boron nitride (hBN)-encapsulated five-layer $NbSe_2$ sample used for magneto-transport measurements. Figure 1g shows device 2 (schematic, Fig. 1h), a magnetic tunnel junction that consists of a normal metal (Pt), bilayer $CrBr_3$ and trilayer $NbSe_2$. $CrBr_3$ with H-stacking is a magnetic semiconductor[26,27] (gap of 0.6–3.8 eV; ref. [28]) with a ferromagnetic ordering temperature of 36 K (ref. [29]) and a magnetic

[1]School of Physics and Astronomy, University of Minnesota, Minneapolis, MN, USA. [2]Department of Physics, The Pennsylvania State University, University Park, PA, USA. [3]Department of Physics and School of Applied and Engineering Physics, Cornell University, Ithaca, NY, USA. [4]National Laboratory of Solid State Microstructures, School of Physics and Collaborative Innovation Center of Advanced Microstructures, Nanjing University, Nanjing, China. [5]National High Magnetic Field Laboratory, Tallahassee, FL, USA. [6]Institute of Condensed Matter Physics, Ecole Polytechnique Fédérale de Lausanne, Lausanne, Switzerland. [7]Kavli Institute at Cornell for Nanoscale Science, Ithaca, NY, USA. [8]These authors contributed equally: Alex Hamill, Brett Heischmidt, Egon Sohn. ✉e-mail: kewang@umn.edu; vpribiag@umn.edu

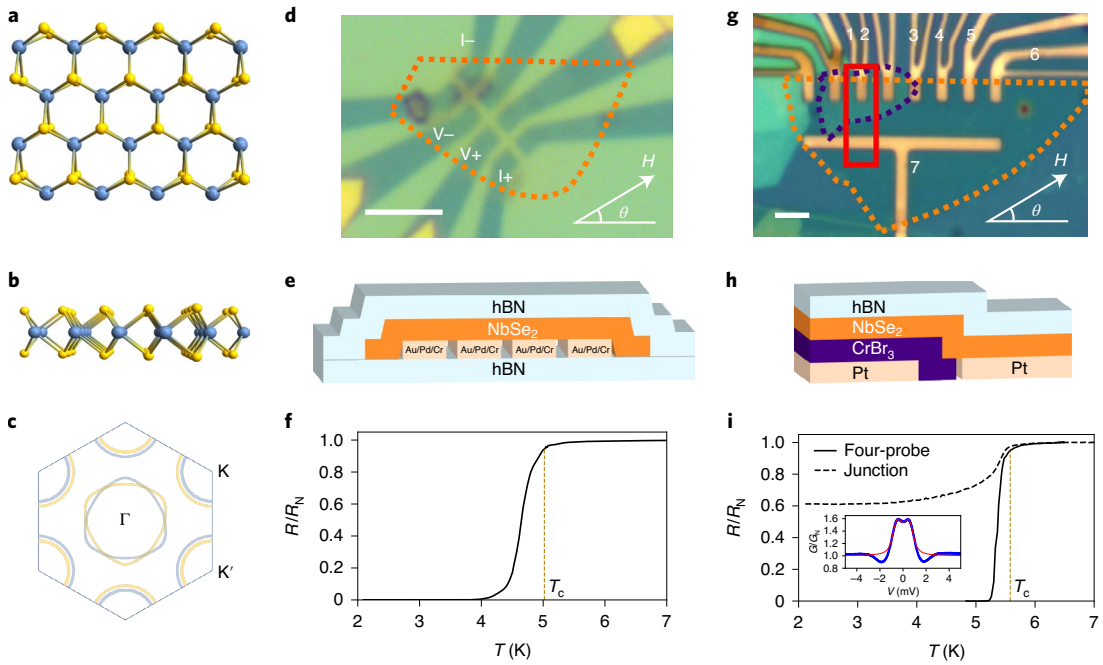

Fig. 1 | Crystal structure, device layout and characterization. a,**b**, Top (**a**) and side (**b**) views of the single-layer 2H-$NbSe_2$ crystal structure. Odd-layer $NbSe_2$ belongs to the point group D_{3h}. **c**, The single-layer $NbSe_2$ Fermi surface in the normal state. The yellow and blue lines represent the spin-up and spin-down split Fermi surfaces. **d**, Optical image of the five-layer $NbSe_2$ device (device 1) used for magnetoresistance measurements. Scale bar, 5 µm. The contacts used for magnetoresistance measurements in Fig. 2 are indicated. **e**, Diagrammatic cross-section of device 1. **f**, Superconducting transition for device 1 ($R_N = 23.6\,\Omega$) at $\mu_0 H = 0$. T_c is defined as the temperature at which $R = 0.95R_N$. **g**, Optical image of the three-layer $NbSe_2$ and bilayer $CrBr_3$ device (device 2) used for junction studies, with the relevant junction highlighted by the red box. Scale bar, 5 µm. Contacts 1, 2, 4 and 7 were used in the junction study. Contacts 3, 4, 5 and 6 were used in the four-probe measurement. For devices 1 and 2, θ is defined as the angle of the magnetic field with respect to the long straight edge of the $NbSe_2$ crystal (orange outline, **d** and **g**). **h**, Diagrammatic cross-section of device 2. **i**, R versus T for device 2, showing the junction resistance ($R_N = 266\,\Omega$) and four-probe resistance ($R_N = 30.6\,\Omega$) at $\mu_0 H = 0$. The junction resistance has a sharp drop at the superconducting transition. Inset: differential conductance (blue) and fit to the Blonder–Tinkham–Klapwijk model (red), indicating a superconducting gap of 0.67 meV, comparable to T_c.

anisotropy field (as reflected by the in-plane saturation field) of ~440 mT (refs. [29–31]). For both types of device, the $NbSe_2$ was exfoliated and encapsulated (see Methods for details) in gloveboxes filled with inert gases (<0.1 ppm O_2 and H_2O concentrations) to preserve a pristine nature for the $NbSe_2$ under study. The same approach was also followed for $CrBr_3$ in the case of the magnetic tunnel junctions.

Figure 1f shows the temperature dependence of the resistance of device 1. The sample shows a clear drop from the normal-state resistance (R_N) to vanishing resistance, with a superconducting transition temperature of $T_c \approx 5.0$ K (defined as the point where $R = 0.9R_N$). This value of T_c is consistent with the value of the superconducting gap Δ extracted from tunnelling data on two-dimensional (2D) $NbSe_2$ (ref. [32]). The device shows transport characteristics similar to those studied in ref. [8]: phonon-limited linear resistance ($R \propto T$) for high temperatures, indicating a metallic sample, and disorder-limited transport (R approaching a plateau) just above the superconducting transition. R_N is defined as the resistance value at this plateau. The resistance remains low (23.6 Ω) just above the superconducting drop, indicating that the sample remains metallic all the way to the superconducting transition. Figure 1i shows similar four-probe data for the magnetic junction sample (device 2). The four-probe resistance of the $NbSe_2$ flake, measured as a function of temperature on a section non-overlapping with the $CrBr_3$ flake, shows a superconducting transition with $T_c \approx 5.5$ K. The zero-bias differential conductance of the junction shows a similar onset temperature; however, the junction resistance saturates towards a finite value of $0.6R_N$ due to the finite resistance of the $CrBr_3$ bilayer in series with the $NbSe_2$. The inset of Fig. 1i shows the differential conductance ($G = \mathrm{d}I/\mathrm{d}V$) of the junction versus d.c. bias at $T = 1.9$ K, with G normalized relative to the normal-state value G_N. We fit the spectrum with the Blonder–Tinkham–Klapwijk model, which considers both quasiparticle tunnelling and Andreev reflection processes[33,34]. The experimental data agree well with the fit, except for the dip observed outside the superconducting gap. The small dip can be attributed to local heating in junctions with high transparency[35]. The superconducting gap of ~0.67 meV extracted from this fit is comparable to the T_c value extracted from the resistance measurements.

Next, we discuss the magneto-transport properties of device 1, probed under an in-plane magnetic field. Care was taken to rule out the effects of an accidental out-of-plane component of the field (Supplementary Sections 1–3 and 5). As the magnetic field is rotated in-plane ($\theta = 0$ corresponds to magnetic field alignment along the $NbSe_2$ flake's longest straight edge), we observe a pronounced two-fold modulation of the magnetoresistance in the range between the onset and the offset of superconductivity (Fig. 2a–e), which is consistent across multiple samples. Such a modulation is well described by a sinusoidal function of the form $\cos(2\theta + \varphi)$ (where φ is the relative phase from $\theta = 0$), as shown by the solid lines. As we varied the temperature for a fixed applied field amplitude of 8 T, the angular modulation of the resistance (ΔR) was suppressed when the resistance was outside the superconducting transition region (Fig. 2d). The phase of the oscillating signal also shifted slightly in device 1 as a function of field and temperature (most apparent in Fig. 2b,e). The field angles at which the resistance maxima or minima were observed were not affected by the directions of voltage measurement, current and material transfer. However, the field

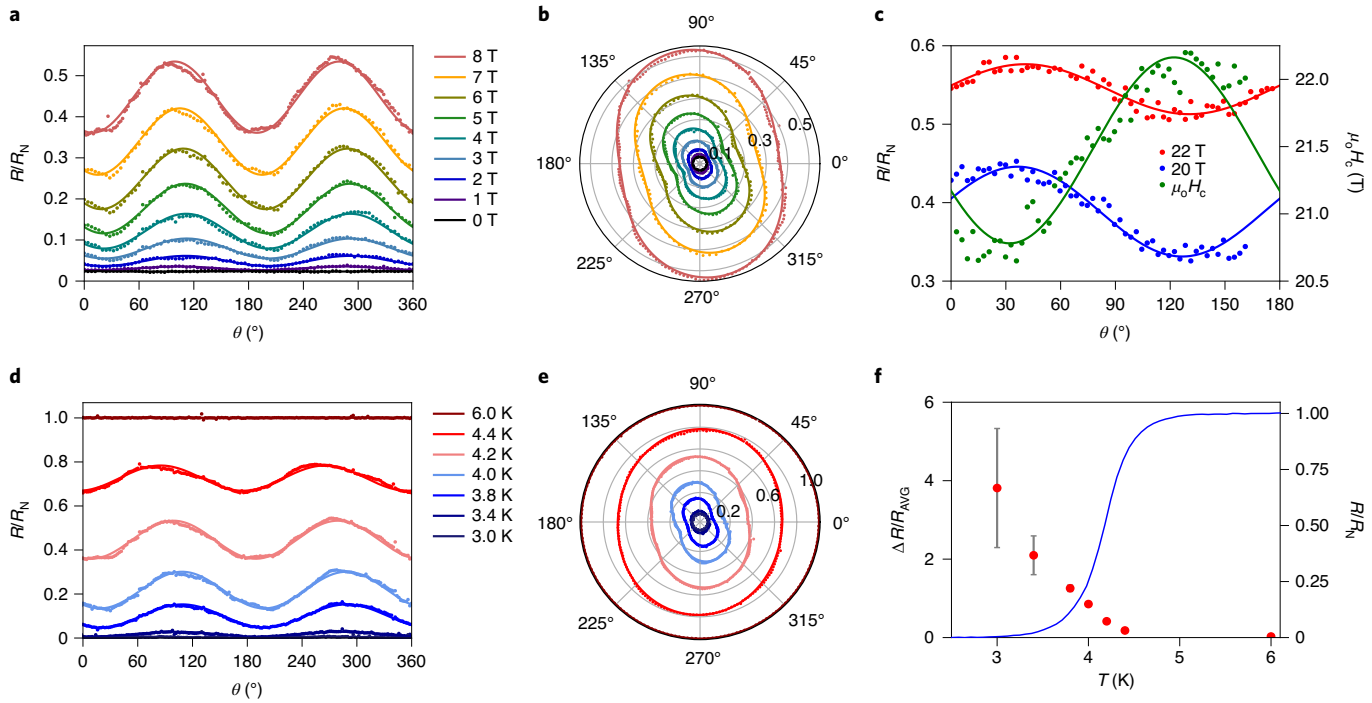

Fig. 2 | Magnetoresistance and effective critical field signatures of two-fold superconducting behaviour. a, Field dependence ($T=4.2$ K) of the magnetoresistance for device 1. **b**, Radial plot of the data in **a** (the radial scale is R/R_N). **c**, Effective critical field (green, right axis) and magnetoresistance characterization (blue and red, left axis) for device 3, five-layer $NbSe_2$ ($R_N=22.2\,\Omega$, $T=0.5$ K). For device 3, θ is defined with respect to an arbitrary reference. **d**, Temperature dependence ($\mu_0H=8$ T) of the magnetoresistance for device 1. **e**, Radial plot of the data in **d**. Solid lines in **a**–**e** are fits to a $\cos(2\theta+\varphi)$ form. **f**, Relative amplitude ($\Delta R/R_{AVG}$) of the magnetoresistance oscillations shown in **d**. A plot of R/R_N versus T for device 1 in the presence of $\mu_0H=8$ T is plotted in blue (right axis). The error bars were calculated using conventional error propagation; the uncertainty of a single data point from **d** was defined as the standard deviation of the 6 K data.

angle of minimum resistance does show a consistent alignment with the long straight edge of the crystal (Supplementary Section 5). We expect that the long straight edge may be associated with the direction of cleaving during exfoliation, which may align along one of the three equivalent zigzag (**a**) or armchair (**b**) directions.

The measurements described above were performed around T_c, in a temperature regime where superconducting fluctuations are present. To verify that this effect persists at lower temperatures, a similar five-layer device (device 3, $T_c\approx6.4$ K) was studied at a temperature of 0.5 K in fields up to ~35 T, revealing a similar modulation of the magnetoresistance with applied field angle (Fig. 2c and Supplementary Fig. 4). For this device, we also studied the angular dependence of the effective critical field $\tilde{H}_c$ that suppresses superconductivity, defined as the field at which the resistance is $0.5R_N$ (measured at $T=0.5$ K). $\tilde{H}_c$ also showed two-fold periodicity (Fig. 2c). The oscillations of $\tilde{H}_c$ and the magnetoresistance have a π phase shift, such that at angles where superconductivity is hardest to suppress, $\tilde{H}_c$ is largest and the magnetoresistance is lowest, as expected. Importantly, these data indicate that the angle dependence of the magnetoresistance is a good proxy for the angle dependence of $\tilde{H}_c$.

To examine the possibility that small out-of-plane field contributions arising from misalignment could lead to these observations, the magneto-transport measurements were repeated in a canted configuration where the sample was intentionally canted by ~7 to 9° out of the field rotation plane. The magnetoresistance oscillations in the canted configuration show a $|\sin(\theta)|$ form, as expected from geometric considerations, which is in contrast with the $\cos(2\theta+\varphi)$ dependence reported in the absence of canting (Supplementary Section 1). Moreover, the amplitude of the two-fold anisotropy would require a canting angle well above our experimental uncertainty (Supplementary Section 2). Another possible experimental effect that could in principle lead to a two-fold modulation in certain cases is current-induced vortex motion[36]. This is ruled out by investigating different contact configurations, as well as by the low current densities employed and the absence of characteristic features of vortex motion in the R versus T curves (Supplementary Sections 5, 6, 8 and 9). More generally, we expect orbital effects to be weak in the few-layer limit of our samples[32]. Even if a weak orbital effect were present, it would not account for the observed two-fold anisotropy because its angular dependence would be expected to follow the in-plane cross-section of the $NbSe_2$ flakes along the field direction, which is inconsistent with our observations on samples with distinct shapes (Supplementary Fig. 5). The robustness of the observations is further supported by recent independent work[37].

As a complementary probe of the two-fold anisotropy deep inside the superconducting state, we also studied the $NbSe_2/CrBr_3$ junction (device 2). In particular, we measured the differential conductance spectra under a 3 T in-plane magnetic field as a function of the angle θ, defined in the same manner as for device 1. At 3 T, the value of the applied field is expected to be substantially larger than the in-plane saturation field (~440 mT)[29] for few-layer $CrBr_3$, ensuring that its spins are oriented in the plane. Figure 3a summarizes the spectra in a colour plot and shows a clear two-fold modulation, especially prominent at a voltage bias smaller than or comparable to the superconducting gap. The angular dependence of the differential conductance at a fixed bias shows a clear contrast between biases larger or smaller than the gap (Fig. 3b). The normalized differential conductance at energies outside the gap ($V=4$ mV$>\Delta/e$) has less than a 0.5% variation versus angle, indicating negligible anisotropic differential conductance. By contrast, the angular dependence of the normalized conductance at energies inside the gap ($V=0$ mV) shows a clear two-fold modulation that can be fit

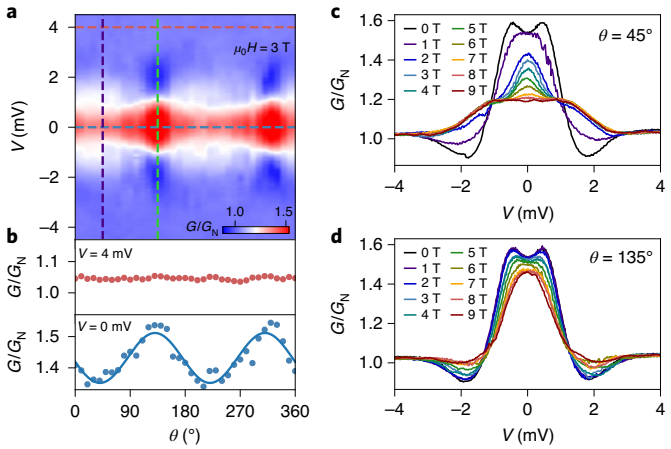

Fig. 3 | Differential conductance spectra under an in-plane magnetic field. **a**, Colour plot of the normalized differential conductance ($G = dI/dV$, G_N corresponding to the normal-state value) of the trilayer $NbSe_2$/bilayer $CrBr_3$/Pt junction (device 2) as a function of the angle θ of the in-plane magnetic field ($\mu_0H = 3$ T, $T = 1.9$ K). **b**, G/G_N versus θ at $V = 0$ and 4 mV (blue and red dashed lines in **a**). The solid line is the best fit to a $\cos(2\theta + \varphi)$ form. **c**,**d**, Field-dependent differential conductance spectra at two fixed in-plane field directions: $\theta = 45°$ (**c**, purple dashed line in **a**) and 135° (**d**, green dashed line in **a**).

to a $\cos(2\theta + \varphi)$ form (solid curve, Fig. 3b). Overall, this indicates that the two-fold modulation persists deep inside the superconducting state of $NbSe_2$, consistent with the magnetoresistance and $\tilde{H}_c$ behaviours. The direction of minimum conductance is slightly rotated from the long, straight edge, which may be due to the additional transfer steps involved. We also studied a second type of junction with a ferromagnetic (Co/Pt multilayer) electrode and an AlO_x barrier (Supplementary Section 11). The Co/Pt junction devices all show alignment of the conductance extrema along the long, straight edge of the $NbSe_2$ flake, similar to the magneto-transport devices.

The differential conductance spectra at $\theta = 45°$ and 135° (Fig. 3c,d) show the angular variation of the spectra versus field amplitude for the CrB_3 tunnel junction. At $H = 0$, we observe a large differential conductance at low bias, approaching 1.6 times the normal-state value. This is due to a combination of Andreev reflection and quasiparticle tunnelling at the junction. When a finite magnetic field is directed along $\theta = 45°$, the differential conductance becomes greatly suppressed. By contrast, when the magnetic field is directed along $\theta = 135°$, the conductance does not change appreciably compared to that of 0 T, indicating a higher resilience of the superconducting state to magnetic fields at this angle and highlighting the two-fold anisotropy of this state. Note that, due to the ferromagnetism of $CrBr_3$, we expect magnetic proximity to be present at the $CrBr_3/NbSe_2$ interface[38], enhancing the effect of the applied magnetic field. In previous studies by some of the authors[34], we investigated over 10 bilayer and trilayer $NbSe_2$ tunnel junctions with nonmagnetic insulating barriers and electrodes and observed a monotonically decreasing gap from zero field up to the upper critical field (~38 T). Any out-of-plane magnetic field due to misalignment would also lead to a monotonically decreasing gap and therefore cannot result in the large suppression of zero-bias differential conductance and widening of the spectra under a magnetic field as observed in this study (Fig. 3c). Within our signal-to-noise ratio, in the nonmagnetic junctions we did not observe a clear in-plane two-fold angle dependence for the tunnelling spectrum under the studied angular magnetic field range (0–9 T). Thus, the strong two-fold angular periodicity of the tunnelling spectra in the low-field limit is unique to devices where the insulating barrier or tunnel electrode are magnetic (Fig. 3 and Supplementary Section 11). However, we cannot exclude such dependence near the upper critical field (>20 T) of the nonmagnetic tunnel devices. Given the two-fold dependence of the upper critical field shown here (Fig. 2c), a two-fold dependence for tunnelling in nonmagnetic junctions is also expected. Interestingly, in all nonmagnetic junctions, the spectra evolved in a manner qualitatively identical to that in Fig. 3d, further suggesting that magnetic proximity coupling plays a role in the magnetic junctions.

Having experimentally established the two-fold anisotropic character of the superconducting state of few-layer $NbSe_2$, we now discuss its possible origin. One scenario is that the superconducting state spontaneously breaks the three-fold rotational symmetry of the lattice; that is, it is a nematic pairing state, similar to that observed in doped Bi_2Se_3 (ref. [39]). This is only possible if two conditions are satisfied: (1) the gap function transforms as the E' or E'' irreducible representations of the D_{3h} point group associated with the single-layer $NbSe_2$ crystal structure (which correspond roughly to *d*-wave and *p*-wave gaps, respectively) and (2) the *d*-wave/*p*-wave nematic gap configuration has a lower energy than the *d*-wave/*p*-wave chiral gap configuration. However, the facts that the superconducting state of bulk $NbSe_2$ is *s*-wave[13] (that is, it transforms as the A_1' irreducible presentation of D_{3h}) and that T_c seems to continuously and slowly change as a function of the number of layers[8] pose a considerable challenge to this scenario.

So, how could an *s*-wave pairing state display two-fold anisotropy? One obvious possibility is extrinsic effects. However, as discussed above, this is difficult to reconcile with the fact that the same sizable two-fold anisotropy is observed for different contact configurations in devices with different geometries, fabricated independently in two separate laboratories and measured using two complementary experimental techniques (magneto-transport and tunnelling). We also consider the possibility of charge density wave (CDW) order. The CDW in both bulk and monolayer $NbSe_2$ is a 3×3 charge order, which does not break the three-fold symmetry of the lattice[10]. As a result, it is not expected to give rise to a two-fold signal. Moreover, CDW onsets above superconductivity[10] and therefore, if it were the origin of the two-fold signal, we would expect to see the anisotropy well above T_c.

Although the origin of this unexpected effect remains an open question, we put forward one possible scenario. This is rooted in the fact that a small external symmetry-breaking field induces a strong mixing between the leading *s*-wave (A_1') instability and a sub-leading instability with either *d*-wave (E') or *p*-wave (E'') character. Such a strong mixing is of course only possible if these sub-leading instabilities of unconventional character, which presumably are accentuated in few-layer $NbSe_2$ by the prominent role played by the Ising SOC, are close competitors of the conventional *s*-wave instability, which is probably inherited from the pairing mechanism of the crystal in bulk form. Note that the mixing discussed here is different from the singlet–triplet mixing that naturally occurs due to the presence of the Ising SOC in the absence of external fields (Supplementary Section 12). In our set-up, two strong candidates exist for such an external symmetry-breaking field. Uniaxial strain mixes the singlet *s*-wave (A_1') and *d*-wave (E') gaps[40,41], giving rise to an overall two-fold anisotropic gap. This is illustrated in Fig. 4b, which shows the mixed gap along the Γ Fermi surface shown in Fig. 1c (details are presented in Supplementary Section 12). Its two-fold anisotropy contrasts with the six-fold anisotropy of the *s*-wave gap shown in Fig. 4a. Experimentally, residual uniaxial strain could arise due to the exfoliation or encapsulation processes, for example. The applied in-plane magnetic field itself also mixes different gap states, as was shown in ref. [17]: due to the presence of the Ising SOC, it mixes the singlet component of the *s*-wave (A_1') gap with the triplet component of the *p*-wave (E'') gap, giving rise to a two-fold symmetric gap, as illustrated in

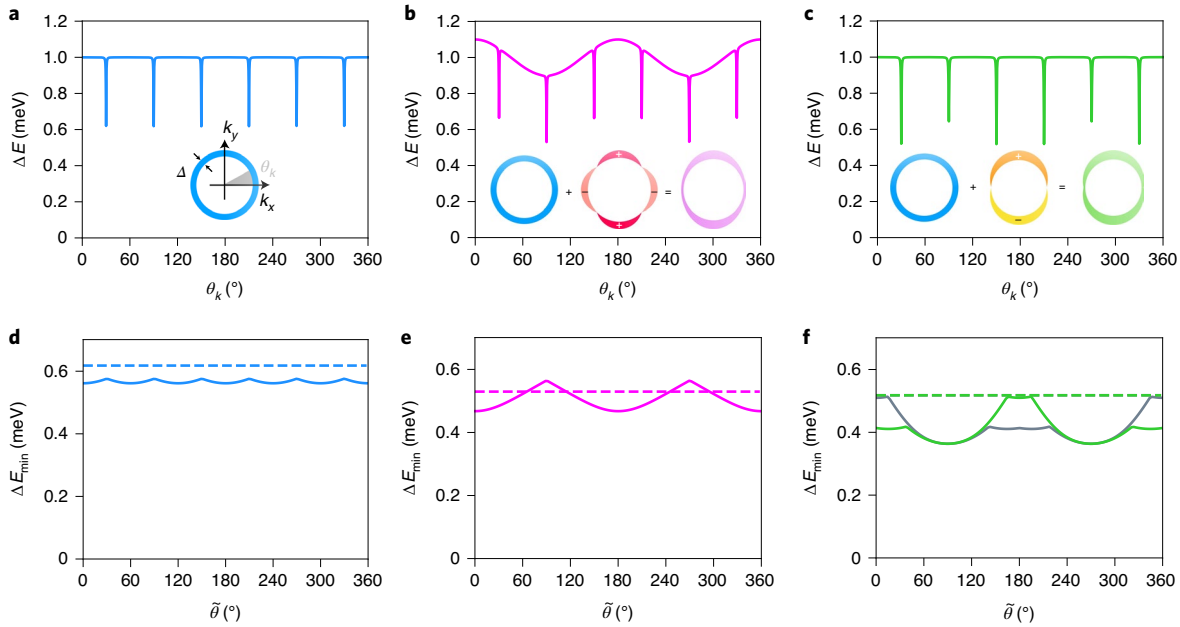

Fig. 4 | Theoretical model for the two-fold anisotropic gap in $NbSe_2$. All gaps refer to the Γ Fermi surfaces shown in Fig. 1c. Although two Fermi pockets exist, the gaps are essentially equal in both, except for **f**. **a**, The A_1' (*s*-wave) gap function. The six-fold anisotropy is a consequence of the Ising SOC and reflects the three-fold rotational symmetry of the lattice. **b**, Mixing of the A_1' (*s*-wave) and E' (*d*-wave) gaps promoted by uniaxial strain applied along the *x* axis. **c**, Mixing of the A_1' (*s*-wave) and E'' (*p*-wave) gaps promoted by the in-plane magnetic field. Insets in **a**–**c**: schematics of the superconducting gaps A_1' (blue), E' (red), E'' (yellow), $A_1' + E'$ (magenta) and $A_1' + E''$ (green). **d**–**f**, Minimum values of the gap function versus real-space angle $\tilde{\theta}$ between the applied *B* field and the *x* axis, obtained by including the Rashba SOC in the gaps displayed in **a**–**c**, respectively. The dashed lines correspond to the case without Rashba SOC. The minimum gap in the pure *s*-wave case, A_1' (**d**), shows a six-fold symmetry with a weak modulation amplitude. By contrast, in **e**, which refers to the $A_1' + E'$ case, the gap minimum has two-fold symmetry. In **f**, corresponding to the $A_1' + E'$ case, the gaps on the two different Γ Fermi pockets are plotted. Note that the minimum of the two gaps displays a two-fold symmetry.

Fig. 4c. We found that the two-fold anisotropy of the $s+p$ mixed state is generally weaker than in the $s+d$ mixed state. Note that the sharp minima in the figure are a consequence of the vanishing of the Ising SOC along the Γ−M direction. Insets in Fig. 4 provide cartoon pictures of the possible $s+p$ ($A_1' + E''$) and $s+d$ ($A_1' + E'$) mixed states and their underlying symmetry-breaking fields.

Although Fig. 4 shows a two-fold anisotropy of the gap in momentum space, an important question is how this is translated into a two-fold anisotropy as a function of the magnetic field orientation. As discussed in Supplementary Section 12, this might be explained by the Rashba SOC that is present due to the existence of a substrate. This is illustrated in Fig. 4d–f, which shows that the minimum value of the gap function of Fig. 4b,c displays a two-fold anisotropy as the magnetic field is rotated in the plane, as long as the Rashba SOC is non-zero (solid lines). By contrast, the minimum gap of Fig. 4a (*s*-wave) shows a six-fold anisotropy. Without the Rashba SOC, the gap minimum is isotropic as a function of the magnetic field angle (dashed lines, Fig. 4d–f). Although a microscopic calculation connecting the anisotropic magnetoresistance, the effective critical field and tunnelling data presented here with a specific form of the gap function is beyond the scope of this work, we expect that the two-fold anisotropy of the mixed gap function—and of the corresponding spectrum of superconducting fluctuations[42]—will be generally manifested as two-fold anisotropic superconducting properties. In the case that a quasi-degeneracy exists between the $s+p$ states or the $s+d$ states, these two-fold anisotropic properties may become pronounced enough to be experimentally detectable, thus explaining our data. We emphasize that the focus of this work is the unexpected experimental observation of the two-fold modulation of the magnetoresistance, effective critical field and tunnel junction conductance by an in-plane magnetic field. Having analysed and ruled out several possible scenarios for these observations, we find that our proposed model accounts for the data very well.

Regardless of which scenario is realized here—spontaneous nematic superconductivity or strong gap-mixing triggered by a small symmetry-breaking field—our results suggest a substantial contribution of an unconventional pairing mechanism to the superconducting state of few-layer $NbSe_2$. This raises fundamental questions about the origin of such pairing interactions, and opens up fascinating prospects of combining them with non-trivial topological properties that have been predicted in the regime of high magnetic fields. Overall, our work reveals that few-layer TMDs provide a promising framework to realize and explore unconventional superconductivity.

Online content

Any methods, additional references, Nature Research reporting summaries, source data, extended data, supplementary information, acknowledgements, peer review information; details of author contributions and competing interests; and statements of data and code availability are available at https://doi.org/10.1038/s41567-021-01219-x.

Received: 14 April 2020; Accepted: 5 March 2021;
Published online: 15 April 2021

References

1. Revolinsky, E., Lautenschlager, E. P. & Armitage, C. H. Layer structure superconductor. *Solid State Commun.* **1**, 59–61 (1963).
2. Xiao, D. et al. Coupled spin and valley physics in monolayers of MoS_2 and other group-VI dichalcogenides. *Phys. Rev. Lett.* **108**, 196802 (2012).
3. Mak, K. F., He, K., Shan, J. & Heinz, T. F. Control of valley polarization in monolayer MoS_2 by optical helicity. *Nat. Nanotechnol.* **7**, 494–498 (2012).

4. Zeng, H., Dai, J., Yao, W., Xiao, D. & Cui, X. Valley polarization in MoS_2 monolayers by optical pumping. *Nat. Nanotechnol.* **7**, 490–493 (2012).
5. Mak, K. F., McGill, K. L., Park, J. & McEuen, P. L. The valley Hall effect in MoS_2 transistors. *Science* **344**, 1489–1492 (2014).
6. Jones, A. M. et al. Spin-layer locking effects in optical orientation of exciton spin in bilayer WSe_2. *Nat. Phys.* **10**, 130–134 (2014).
7. Riley, J. M. et al. Direct observation of spin-polarized bulk bands in an inversion-symmetric semiconductor. *Nat. Phys.* **10**, 835–839 (2014).
8. Xi, X. et al. Ising pairing in superconducting $NbSe_2$ atomic layers. *Nat. Phys.* **12**, 139–143 (2016).
9. Xu, X., Yao, W., Xiao, D. & Heinz, T. F. Spin and pseudospins in layered transition metal dichalcogenides. *Nat. Phys.* **10**, 343–350 (2014).
10. Ugeda, M. M. et al. Characterization of collective ground states in single-layer $NbSe_2$. *Nat. Phys.* **12**, 92–97 (2016).
11. Moncton, D. E., Axe, J. D. & DiSalvo, F. J. Neutron scattering study of the charge-density wave transitions in 2H-$TaSe_2$ and 2H-$NbSe_2$. *Phys. Rev. B* **16**, 801–819 (1977).
12. Harper, J. M. E., Geballe, T. H. & DiSalvo, F. J. Thermal properties of layered transition-metal dichalcogenides at charge-density-wave transitions. *Phys. Rev. B* **15**, 2943–2951 (1977).
13. Fletcher, J. D. et al. Penetration depth study of superconducting gap structure of 2H-$NbSe_2$. *Phys. Rev. Lett.* **98**, 057003 (2007).
14. De La Barrera, S. C. et al. Tuning Ising superconductivity with layer and spin–orbit coupling in two-dimensional transition-metal dichalcogenides. *Nat. Commun.* **9**, 1427 (2018).
15. Clogston, A. M. Upper limit for the critical field in hard superconductors. *Phys. Rev. Lett.* **9**, 266–267 (1962).
16. Chandrasekhar, B. S. A note on the maximum critical field of high-field superconductors. *Appl. Phys. Lett.* **1**, 7–8 (1962).
17. Möckli, D. & Khodas, M. Magnetic-field induced $s+if$ pairing in Ising superconductors. *Phys. Rev. B* **99**, 180505 (2019).
18. Möckli, D. & Khodas, M. Robust parity-mixed superconductivity in disordered monolayer transition metal dichalcogenides. *Phys. Rev. B* **98**, 144518 (2018).
19. Yuan, N. F. Q., Mak, K. F. & Law, K. T. Possible topological superconducting phases of MoS_2. *Phys. Rev. Lett.* **113**, 097001 (2014).
20. Samokhin, K. V. Symmetry and topology of two-dimensional noncentrosymmetric superconductors. *Phys. Rev. B* **92**, 174517 (2015).
21. Zhou, B. T., Yuan, N. F. Q., Jiang, H. L. & Law, K. T. Ising superconductivity and Majorana fermions in transition-metal dichalcogenides. *Phys. Rev. B* **93**, 180501 (2016).
22. Hsu, Y. T., Vaezi, A., Fischer, M. H. & Kim, E. A. Topological superconductivity in monolayer transition metal dichalcogenides. *Nat. Commun.* **8**, 14985 (2017).
23. He, W.-Y. et al. Magnetic field driven nodal topological superconductivity in monolayer transition metal dichalcogenides. *Commun. Phys.* **1**, 40 (2018).
24. Fischer, M. H., Sigrist, M. & Agterberg, D. F. Superconductivity without inversion and time-reversal symmetries. *Phys. Rev. Lett.* **121**, 157003 (2018).
25. Shaffer, D., Kang, J., Burnell, F. J. & Fernandes, R. M. Crystalline nodal topological superconductivity and Bogolyubov Fermi surfaces in monolayer $NbSe_2$. *Phys. Rev. B* **101**, 224503 (2020).
26. Tsubokawa, I. On the magnetic properties of a $CrBr_3$ single crystal. *J. Phys. Soc. Jpn* **15**, 1664–1668 (1960).
27. Ghazaryan, D. et al. Magnon-assisted tunnelling in van der Waals heterostructures based on $CrBr_3$. *Nat. Electron.* **1**, 344–349 (2018).
28. Baral, D. et al. Small energy gap revealed in $CrBr_3$ by scanning tunneling spectroscopy. *Phys. Chem. Chem. Phys.* **23**, 3225–3232 (2021).
29. Kim, H. H. et al. Evolution of interlayer and intralayer magnetism in three atomically thin chromium trihalides. *Proc. Natl Acad. Sci. USA* **166**, 11131–11136 (2019).
30. Zhang, Z. et al. Direct photoluminescence probing of ferromagnetism in monolayer two-dimensional $CrBr_3$. *Nano Lett.* **19**, 3138–3142 (2019).
31. Chen, W. et al. Direct observation of van der Waals stacking–dependent interlayer magnetism. *Science* **366**, 983–987 (2019).
32. Dvir, T. et al. Spectroscopy of bulk and few-layer superconducting $NbSe_2$ with van der Waals tunnel junctions. *Nat. Commun.* **9**, 598 (2018).
33. Blonder, G. E., Tinkham, M. & Klapwijk, T. Transition from metallic to tunneling regimes in superconducting microconstrictions: excess current, charge imbalance and supercurrent conversion. *Phys. Rev. B* **25**, 4515–4532 (1982).
34. Sohn, E. et al. An unusual continuous paramagnetic-limited superconducting phase transition in 2D $NbSe_2$. *Nat. Mater.* **17**, 504–508 (2018).
35. Sheet, G., Mukhopadhyay, S. & Raychaudhuri, P. Role of critical current on the point-contact Andreev reflection spectra between a normal metal and a superconductor. *Phys. Rev. B* **69**, 134507 (2004).
36. Wang, Y. L. et al. Parallel magnetic field suppresses dissipation in superconducting nanostrips. *Proc. Natl Acad. Sci. USA* **114**, E10274–E10280 (2017).
37. Cho, C. et al. Distinct nodal and nematic superconducting phases in the 2D Ising superconductor $NbSe_2$. Preprint at https://arxiv.org/pdf/2003.12467.pdf (2020).
38. Cai, X. et al. Disentangling spin–orbit coupling and local magnetism in a quasi-two-dimensional electron system. *Phys. Rev. B* **100**, 081402(R) (2019).
39. Matano, K., Kriener, M., Segawa, K., Ando, Y. & Zheng, G. Q. Spin–rotation symmetry breaking in the superconducting state of $Cu_xBi_2Se_3$. *Nat. Phys.* **12**, 852–854 (2016).
40. Fernandes, R. M. & Millis, A. J. Nematicity as a probe of superconducting pairing in iron-based superconductors. *Phys. Rev. Lett.* **111**, 127001 (2013).
41. Kang, J., Kemper, A. F. & Fernandes, R. M. Manipulation of gap nodes by uniaxial strain in iron-based superconductors. *Phys. Rev. Lett.* **113**, 217001 (2014).
42. Venderbos, J. W. F., Kozii, V. & Fu, L. Identification of nematic superconductivity from the upper critical field. *Phys. Rev. B* **94**, 094522 (2016).

Methods

Device fabrication. For the magneto-transport and effective critical field measurement devices, Cr/PdAu (1 nm/7 nm) bottom contacts were deposited on top of an atomically clean piece of hBN of thickness 20–80 nm, above which pieces of 2H-$NbSe_2$ (commercial, from HQ Graphene) and hBN (20–80 nm) was subsequently transferred using the standard dry-transfer technique[43]. The $NbSe_2$ layer number was determined via optical contrast[44] calibrated by atomic force microscopy. The $NbSe_2$ exfoliation and subsequent hBN encapsulation were performed in an Ar-filled glovebox to minimize sample degradation. After completing the assembly process, the van der Waals heterostructure was taken out of the glovebox and etched by reactive ion etching with O_2/Ar/CHF_3 to open windows on the top hBN for contacting the pre-patterned bottom contacts. Metal leads of Cr/Pd/Au (1 nm/5 nm/120 nm) were subsequently deposited to connect the bottom contacts to the bonding pads.

For the junction devices, 2H-$NbSe_2$ bulk single crystals were prepared by the iodine-based chemical vapour transport method. $CrBr_3$ and hBN bulk single crystals were grown by HQ Graphene. $NbSe_2$ and $CrBr_3$ were thinned down by the conventional Scotch tape method and assembled using the dry-transfer technique in a N_2-filled glovebox[43,45]. In detail, both $NbSe_2$ and $CrBr_3$ were first exfoliated on a polydimethylsiloxane (PDMS) polymer substrate. $NbSe_2$ flakes on the PDMS stamp were transferred to a Si/SiO_2 (295 nm) substrate, which was heated to 70 °C. By searching with an optical microscope, trilayer $NbSe_2$ was identified. A stamp with a thin layer of polypropylene carbonate (PPC) on PDMS was prepared on a glass slide. The trilayer $NbSe_2$ was picked up onto the stamp at 45 °C. Thin $CrBr_3$ flakes were identified on the PDMS polymer substrate and aligned to the $NbSe_2$ flake on the stamp. The $CrBr_3$ was picked up from the PDMS substrate onto the stamp at 50 °C. The stack was aligned and approached to a pre-patterned metal electrode at 50 °C followed by heating the substrate to 120 °C to release the stack. The pre-patterned metal electrodes of Ti (3 nm)/Pt (70 nm) were prepared by standard photolithography and electron-beam evaporation. The PPC layer on the device was dissolved by anisole. Finally, the device was single-side-encapsulated by hBN to prevent any degradation in air. All device fabrication procedures occurred in the glovebox.

Measurements. The magnetoresistance measurements for device 1 were performed using a Physical Properties Measurement System equipped with a rotating, variable-temperature sample insert and a 9-T magnet. A standard lock-in technique was used with an a.c. current of 400 nA (3 μA was used for the R versus T plot in Fig. 1f only). Device 3 measurements were performed at the National High Magnetic Field Laboratory (NHMFL), using a standard lock-in technique in a ^{3}He cryostat equipped with a rotating sample insert and a 35-T d.c. magnet. For the measurements at NHMFL, an a.c. current of 1 μA was used.

The junction devices were measured in a separate 9-T Physical Property Measurement System at 1.9 K. A rotating probe was used to apply an in-plane magnetic field at angle θ. For the four-probe transport measurement of $NbSe_2$, we chose four electrodes, which were in direct contact with $NbSe_2$ regions (not covered by $CrBr_3$). A standard lock-in technique was used with an a.c. current of 1 μA. For the differential conductance measurements, a small a.c. current and d.c. bias current were generated by a lock-in amplifier and a d.c. voltage source meter, respectively, with load resistances in series. The superimposed current flowed through one of the split electrodes of the junction. The a.c. and d.c voltages were measured between the other split electrode and another remote electrode using a pre-amplifier, lock-in amplifier and a voltage meter (see Supplementary Section 10 for the measurement schematics). The amplitude of the a.c. voltage was kept below 50 μV and the d.c. voltage was varied from −8 mV to 8 mV. The differential conductance G was calculated from the ratio of the a.c. current to the measured a.c. voltage. The bias voltage V in the main text corresponds to the measured d.c. voltage.

Data availability

Data for figures (including Supplementary figures) are available in the public repository Zenodo at https://doi.org/10.5281/zenodo.4545917. Source data are provided with this paper.

Code availability

All relevant codes needed to evaluate the conclusions in the paper are available from the corresponding authors upon reasonable request.

References

43. Castellanos-Gomez, A. et al. Deterministic transfer of two-dimensional materials by all-dry viscoelastic stamping. *2D Mater.* **1**, 011002 (2014).
44. Bing, D. et al. Optical contrast for identifying the thickness of two-dimensional materials. *Opt. Commun.* **406**, 128–138 (2018).
45. Novoselov, K. S. et al. Electric field in atomically thin carbon films. *Science* **306**, 666–669 (2004).

Acknowledgements

We thank E.-A. Kim for useful discussions. B.H. and A.H. thank D. Graf and S. Maier for their discussions and support related to work done at the National High Magnetic Field Laboratory. Special thanks also go to Z. Jiang for all of the support associated with the Physical Property Measurement System at UMN. The work at the University of Minnesota (UMN) was supported primarily by the National Science Foundation through the University of Minnesota MRSEC, under Awards DMR-2011401 and DMR-1420013 (iSuperSeed). Portions of the UMN work were conducted in the Minnesota Nano Center, which is supported by the National Science Foundation through the National Nano Coordinated Infrastructure Network (NNCI) under award no. ECCS-1542202. A portion of this work was performed at the National High Magnetic Field Laboratory, which is supported by National Science Foundation Cooperative agreement no. DMR-1644779 and the State of Florida. The research at Cornell was supported by the Office of Naval Research (ONR) under award no. N00014-18-1-2368 for the tunnelling measurements, and the National Science Foundation (NSF) under award no. DMR-1807810 for the fabrication of tunnel junctions. The work in Lausanne was supported by the Swiss National Science Foundation. K.F.M. also acknowledges support from a David and Lucille Packard Fellowship.

Author contributions

B.H., A.H., V.S.P. and K.W. designed the magnetoresistance and effective critical field experiments. B.H. performed the transport measurements at UMN with support from A.H. and K.-T.T. B.H. and A.H. performed the measurements at the NHMFL with support from A.S. B.H. analysed the data with support from A.H. under the supervision of V.S.P. and K.W. A.H., K.-T.T. and X.Z. fabricated the magneto-transport heterostructures with support from B.H., under the supervision of K.W. Analytical modelling was performed by D.S., R.M.F. and F.J.B., who also contributed to the interpretation of the results. E.S., X.X., J.S. and K.F.M. designed the junction experiments. E.S. and X.X. fabricated and measured the junctions under the supervision of J.S. and K.F.M. E.S. analysed the junction data under the supervision of J.S. and K.F.M., with input from V.S.P. and R.M.F. H.B. and L.F. grew the bulk $NbSe_2$ samples for tunnel junction studies. B.H., A.H., E.S., D.S., V.S.P. and R.M.F. co-wrote the manuscript. All authors discussed the results and provided comments on the manuscript.

Competing interests

The authors declare no competing interests.

Additional information

Supplementary information The online version contains supplementary material available at https://doi.org/10.1038/s41567-021-01219-x.

Correspondence and requests for materials should be addressed to K.W. or V.S.P.

Peer review information *Nature Physics* thanks Hadar Steinberg, Carsten Timm and the other, anonymous, reviewer(s) for their contribution to the peer review of this work.

Reprints and permissions information is available at www.nature.com/reprints.